





Efficient radioactive gas detection by scintillating porous metal–organic frameworks

Received: 15 November 2022

Accepted: 7 April 2023

Published online: 18 May 2023

 Check for updates

Matteo Orfano ^{1,5}, Jacopo Perego^{1,5}, Francesca Cova ¹,
Charl X. Bezuidenhout ¹, Sergio Piva ¹, Christophe Dujardin ²,
Benoit Sabot ³, Sylvie Pierre³, Pavlo Mai², Christophe Daniel ⁴,
Silvia Bracco ¹, Anna Vedda ¹✉, Angiolina Comotti ¹✉ &
Angelo Monguzzi ¹✉

Natural and anthropogenic gas radionuclides such as radon, xenon, hydrogen and krypton isotopes must be monitored to be managed as pathogenic agents, radioactive diagnostic agents or nuclear activity indicators. State-of-the-art detectors based on liquid scintillators suffer from laborious preparation and limited solubility for gases, which affect the accuracy of the measurements. The actual challenge is to find solid scintillating materials simultaneously capable of concentrating radioactive gases and efficiently producing visible light revealed with high sensitivity. The high porosity, combined with the use of scintillating building blocks in metal–organic frameworks (MOFs), offers the possibility to satisfy these requisites. We demonstrate the capability of a hafnium-based MOF incorporating dicarboxy-9,10-diphenylanthracene as a scintillating conjugated ligand to detect gas radionuclides. Metal–organic frameworks show fast scintillation, a fluorescence yield of ~40%, and accessible porosity suitable for hosting noble gas atoms and ions. Adsorption and detection of ⁸⁵Kr, ²²²Rn and ³H radionuclides are explored through a newly developed device that is based on a time coincidence technique. Metal–organic framework crystalline powder demonstrated an improved sensitivity, showing a linear response down to a radioactivity value below 1 kBq m⁻³ for ⁸⁵Kr, which outperforms commercial devices. These results support the possible use of scintillating porous MOFs to fabricate sensitive detectors of natural and anthropogenic radionuclides.

Natural radioactive gases such as the isotopes of radon (²²²Rn and ²²⁰Rn), and the anthropogenic radionuclides coming from fission (¹³³Xe and ⁸⁵Kr) and activation (³H and ³⁷Ar) products, need to be carefully monitored. Isotopes such as ⁸⁵Kr and ³H, which originate from nuclear

power plants, reprocessing plants and nuclear waste treatments^{1–5}, are critical to detect for monitoring nuclear activity and uncovering illegal reprocessing to produce plutonium for weapons⁶. ¹³³Xe and ³⁷Ar are of key interest, as they can be used to detect covert activities to

¹Dipartimento di Scienza dei Materiali, Università degli Studi Milano-Bicocca, Milan, Italy. ²Institut Lumière Matière, Université Claude Bernard Lyon, Lyon, France. ³Université Paris-Saclay, CEA, LIST, Laboratoire National Henri Becquerel (LNE-LNHB), Palaiseau, France. ⁴Nano Active Film SRL, Dipartimento di Chimica e Biologia, Università degli Studi di Salerno, Fisciano, Italy. ⁵These authors contributed equally: Matteo Orfano, Jacopo Perego. ✉e-mail: anna.vedda@unimib.it; angiolina.comotti@unimib.it; angelo.monguzzi@unimib.it

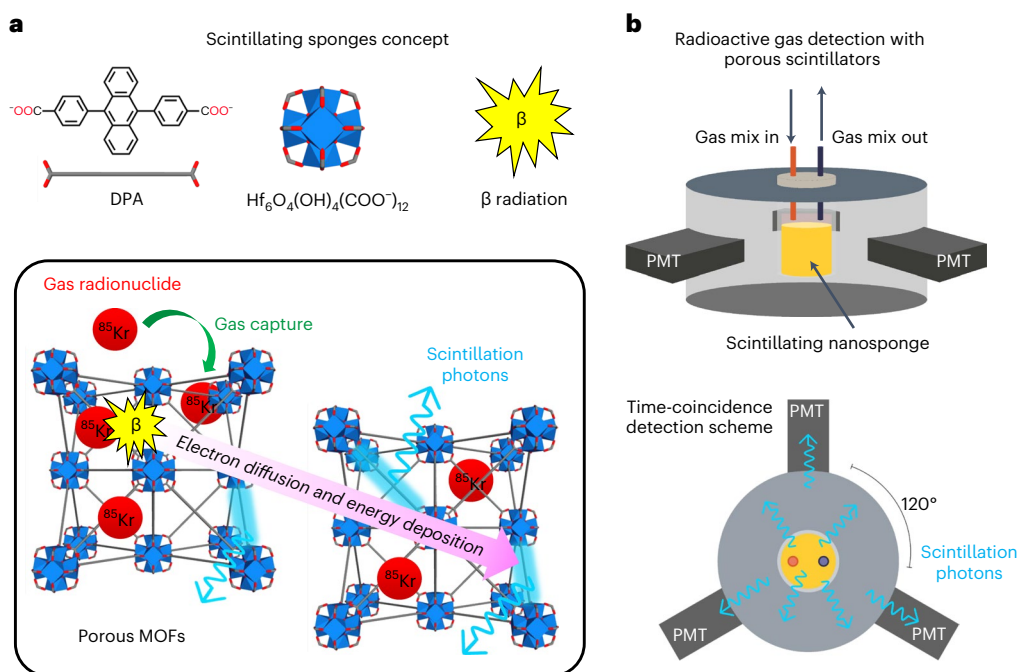


Fig. 1 | Time-coincidence-based detector for radionuclides gases exploiting porous scintillators. **a**, Schematic representation of the scintillation mechanism inside fluorescent hafnium-based MOFs. The porous frameworks can uptake radioactive gaseous species through physical adsorption and concentrate them inside the pores. The decay process produces β -particles that can effectively interact with the porous particles during their diffusion and thermalization, triggering a sensitized scintillation process. The ligand and metal node that constitutes HF-DPA, as well as the β -radiation emitted by radionuclides, are

shown at the top. **b**, Sketch of the triple coincidence system designed to reveal radioactive gases by exploiting a porous scintillator. The porous material is placed in the central chamber where it adsorbs the flowing gas molecules, whose β -decay produces high-energy electrons in the pores. The interactions of electrons with the walls of the pores generate the light pulses to be recorded by three symmetric PMTs employed to have a low-noise, time-coincidence detection.

verify compliance with the Comprehensive Nuclear-Test-Ban Treaty⁷. On the other hand, gases from granite-rich areas (^{222}Rn and ^{220}Rn)^{8–10} are pathogenic agents that must be quantified to mitigate the exposure risk, whereas xenon isotopes are useful as radioactive diagnostic contrast agents to evaluate pulmonary function, lung imaging and cerebral blood flow by inhalation^{11–13}. The detection and radioactivity metrology of gases is thus a crucial aspect in a modern, technologically advanced and sustainable society, as demonstrated by the recurrent updates of regulations that ask for increasingly more sensitive and accurate detectors^{14,15}.

All of the listed radionuclides decay by emitting β -particles (α - and β -particles the case of radon); that is, electrons that are difficult to detect due to their short-range path in matter, especially for ^3H (ref. 16). In this case, the liquid scintillation counting technique is the gold standard to measure radioactivity, but it requires a long and complex procedure to mix ^3H -labelled water with the scintillator¹⁷. This hinders in situ online measurements and produces liquid radioactive waste that must be carefully managed. Moreover, it cannot be applied to other gas radionuclides, which are highly insoluble. In this case the only option is to use gas meters that require large volumes and counting gases to increase the detection efficiency, resulting in very impractical instrumentation (see Supplementary Section 11).

A key solution to bypass these issues is to use solid porous scintillators: the adsorption and accumulation in the pores would concentrate the radionuclide, while simultaneously enhancing the probability of the scintillators interacting with the generated ionizing radiation, thus increasing the device sensitivity. Porous scintillators would allow the use of low detection volumes, thus enabling the realization of practical small instruments for in situ operation. Importantly,

the porous systems can also be cleaned from radioactive species and reused, thus enabling a sustainable technology that reduces risks and costs. Porous scintillators are therefore proposed as a new class of scintillating materials for the development of highly responsive and universal radioactive gas detectors based on time-coincidence techniques (Fig. 1a)¹⁸.

Scintillating metal-organic frameworks (MOFs) endowed with high porosity are excellent candidates. The controlled self-assembly of inorganic nodes and organic ligands produces tailored architectures with well-defined porosity for gas capture, separation and storage^{19–22}. Metal-organic frameworks have also been used as sorbents for the sequestration of noble gases²³ and, in some cases, ion radionuclides²⁴. Luminescent chromophores, included as ligands or guests, can be integrated to build emissive materials with unique photophysical^{25–28} and scintillating properties^{26–28}. However, despite recent MOF developments as colorimetric- and fluorescence-sensing platforms²⁹ and scintillators, their potential application for the detection of gas radioactivity has not yet been reported. Indeed, luminescent MOFs have been used to detect the presence of a few radioactive analytes in solution, but without any correlation to their radioactive properties³⁰.

Here we demonstrate the capability of porous hafnium-based MOFs containing the dicarboxy-9,10-diphenylanthracene (DPA) as a scintillating ligand for gas-radioactivity detection (Fig. 1). The crystalline MOF shows a highly accessible porosity suitable for hosting radioactive gases, which transfer their ionizing radiation to the framework, producing fast scintillation appropriate for time coincidence detection techniques and a good fluorescence quantum yield of $\sim 40\%$. The heavy hafnium improves the interaction with ionizing radiation and enables a good light intensity output, that is, one order of magnitude larger than a commercial scintillator. These excellent properties prompt us to test

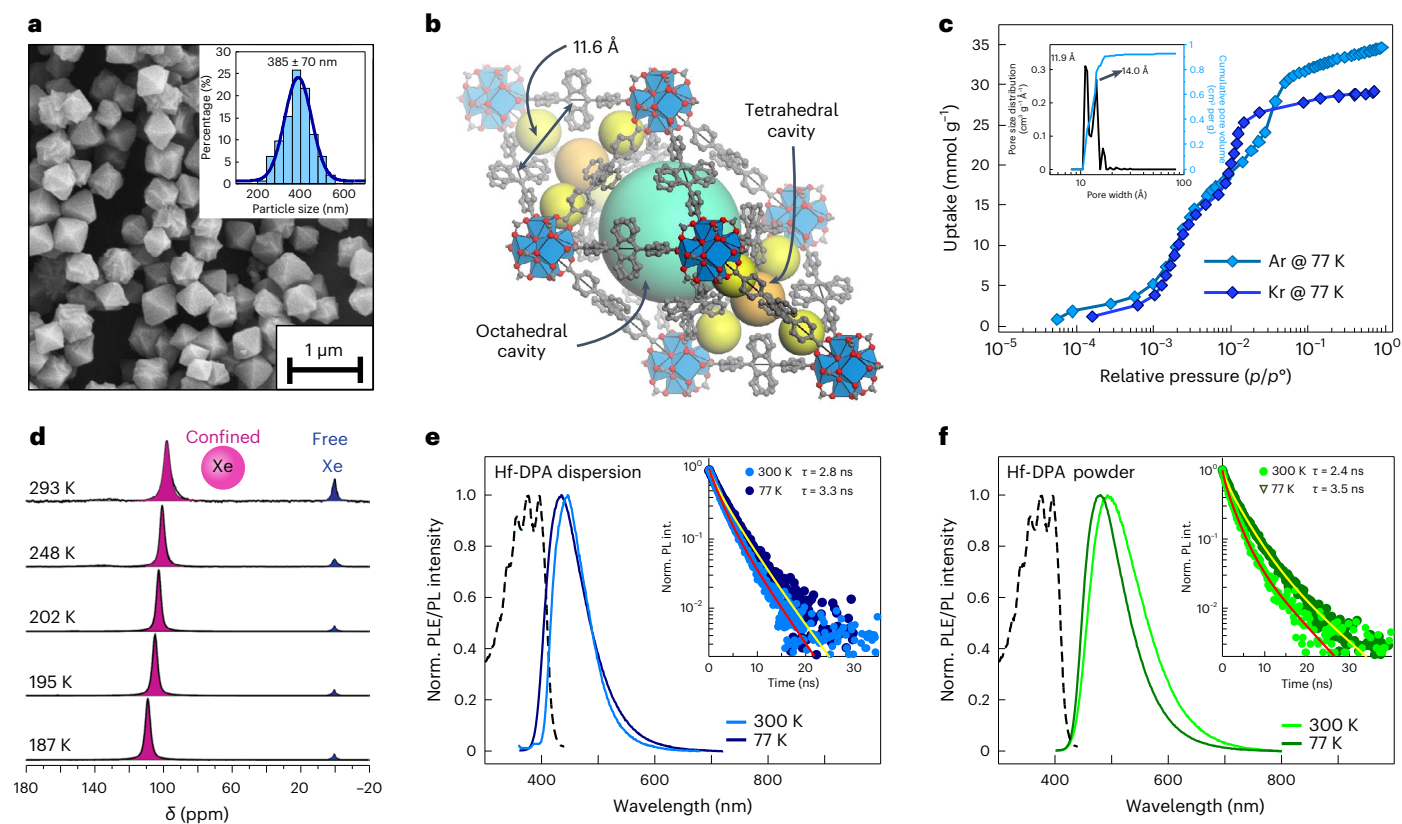


Fig. 2 | Structural, gas adsorption and photoluminescence properties of fluorescent porous MOFs. **a**, Scanning electron microscopy image of Hf-DPA MOFs. The inset depicts the MOF size distribution obtained by SEM image analysis. **b**, Crystal structure of Hf-DPA highlighting the octahedral and tetrahedral cavities. The triangular pore window and centre-to-centre distance between DPA molecules are highlighted. **c**, Argon (light blue) and krypton (dark blue) adsorption isotherms collected at 77 K. Inset: pore size distribution calculated from argon adsorption isotherm using the non-local density functional theory method. **d**, Hyperpolarized ^{129}Xe NMR spectra of Hf-DPA at

variable temperature, 2% xenon in a mixture with nitrogen and helium. **e,f**, The excitation photoluminescence (PLE, dashed line) and photoluminescence (PL) emission spectra of MOF crystals dispersed in THF ($5 \times 10^{-8} \text{ M}$) (**e**) or as bare powder (**f**). The photoluminescence was recorded at 300 K (solid line) and 77 K (dotted line). The excitation wavelength is 355 nm. The insets show the photoluminescence intensity (PL int.) decay as a function of time recorded at the photoluminescence maximum emission wavelength under 340 nm pulsed excitation. The solid lines represent the fit of data with multi-exponential decay functions that results in the average emission lifetime values reported.

the sorption and detection of ^{85}Kr , ^{222}Rn and ^3H radionuclides in a newly developed device that exploits the scintillating MOF powder as a gas harvester and concentrator (Fig. 1a). Metal-organic frameworks show an improved sensitivity with respect to the reference powders currently tested for gas detection, as well as an excellent linear response down to an activity value of below 1 kBq m^{-3} for ^{85}Kr , thus outperforming commercial detectors in a compact, cost effective and easy-to-handle architecture. The combination of porosity, good quantum yield and fast scintillation strongly support the possible use of scintillating porous MOFs as active components to fabricate technologically superior sensors for detecting natural and anthropogenic radioactive gases at ultralow concentrations.

Results

Gas adsorption and photoluminescence properties of Hf-based MOFs

Hafnium-based MOFs comprising luminescent DPA ligands (Hf-DPA) were obtained through solvothermal synthesis (see Methods and Supplementary Figs. 1–7)^{27,28}, which has been optimized to produce octahedral crystals with a cubic crystal structure 385 nm in diameter (Fig. 2a,b)—at which size the emission properties are best—in highly reproducible batches from few tens of milligrams up to ~200 mg (Supplementary Table 1 and Supplementary Figs. 8–20). Low-temperature gas adsorption isotherms demonstrate the microporous nature of Hf-DPA, and the adsorption of noble gases such as argon

and krypton (Fig. 2c and Supplementary Fig. 30). The argon and krypton adsorption isotherms were also measured at room temperature, demonstrating the gas diffusion inside the cavities under pressure and temperature conditions comparable with the operational scenario of radioactive gas detection (Supplementary Fig. 31). In this regard we provide direct detection of noble gas diffusion into the pores of the Hf-DPA by hyperpolarized ^{129}Xe NMR experiments, even in competition with other gaseous species and under flow conditions (Fig. 2d, Methods, Supplementary Table 5 and Supplementary Fig. 28)^{28,31–35}. The detection of the signal at $\delta = 97.7 \text{ ppm}$ within 200 ms demonstrates the fast diffusion in the restricted pores.

Figure 2e shows the steady-state photoluminescence and excitation photoluminescence (PLE) spectra of Hf-DPA dispersed in tetrahydrofuran (see Methods). Under ultraviolet excitation, the dispersion exhibits a blue fluorescence peak at 450 nm, with a characteristic average decay time of 2.8 ns and a photoluminescence quantum yield of 0.41 ± 0.06 (Supplementary Section 7). The broad spectrum mirrors the presence of a distribution of local environments and quenching pathways for the emitting ligands^{25,26,35}. The excitation photoluminescence profile recorded at 450 nm matches the vibronic structure of DPA molecules³⁵. Low-temperature measurements show a blue shift of the photoluminescence maximum to 440 nm, ascribed to the band narrowing at cryogenic temperatures that reduces self-absorption, and an increased decay time of 3.3 ns, which indicates an emission yield increment to $0.41 \times \frac{3.3 \text{ ns}}{2.8 \text{ ns}} = 0.48$ (+18%).

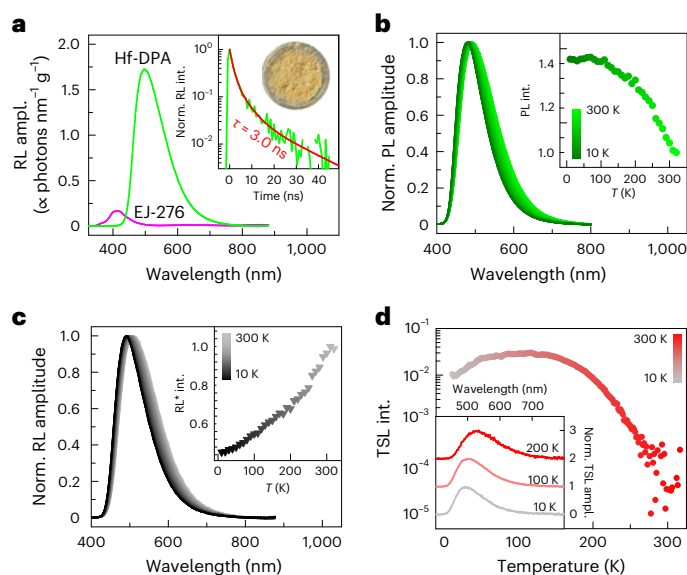


Fig. 3 | Scintillation properties of Hf-DPA MOF powder. **a**, Radioluminescence (RL) spectrum of Hf-MOFs and plastic EJ-276 scintillator powders under soft X-rays. The inset shows the scintillation pulse recorded for Hf-DPAs with a picture of the MOF powder. The solid line represents the fit with a multi-exponential decay function. **b, c**, Normalized PL (**b**) and RL spectra (**c**) of Hf-DPA powders as a function of temperature. The inset in **c** depicts the radioluminescence intensity (RL*) normalized to the PL intensity variation shown in the inset of **b**, as a function of the temperature. **d**, Thermally stimulated luminescence intensity of Hf-DPA crystals powder as a function of the temperature, that is, the glow curve, obtained by integrating wavelength resolved measurements in the whole emission region. The inset depicts representative TSL spectra recorded at 10 K, 100 K and 200 K.

This confirms the absence of substantial thermal quenching in Hf-DPA by intramolecular vibrational mechanisms^{25,26,35}. Figure 2f reports the photoluminescence properties of the Hf-DPA powder that will be used to detect the gas radionuclides. The emission at room temperature is red shifted to 490 nm due to the larger inner filter effect of self-absorption in the powder, whereas the PLE profile matches that of MOF in THF. The emission lifetime of 2.4 ns is basically unchanged. At 77 K, the emission maximum is again slightly blue shifted to 480 nm with a lifetime increment to 3.5 ns, confirming that the excited state electronic properties of the MOF powder are consistent with those of single crystals in diluted dispersion.

Scintillation properties of Hf-DPA

Figure 3a shows the steady-state scintillation (radioluminescence) spectrum of Hf-DPA powder compared with the commercial plastic scintillator EJ-276 (Methods) under soft X-rays. The MOF powder radioluminescence matches the photoluminescence profile (Fig. 2f). Notably, despite the Hf-DPA density of 0.6–0.7 g cm⁻³ being lower than the 1.1 g cm⁻³ of EJ-276, the scintillation generated by MOFs is more than one order of magnitude intense (Fig. 3a). This is ascribed to the presence of heavy hafnium ions ($Z = 72$) enhancing the interaction with ionizing radiation, which allows the scintillation efficiency of the Hf-DPA to double with respect to the parent zirconium-based MOF (Supplementary Fig. 32)²⁵. Hf-DPA produces a fast scintillation light pulse (Fig. 3a, inset) with a subnanosecond rise time and average decay time of 3 ns, which matches the photoluminescence decay dynamics. This confirms that the MOF emission properties are preserved under X-ray excitation.

The photoluminescence and radioluminescence of Hf-DPA have been monitored against temperature. Figure 3b shows the MOF powder normalized photoluminescence spectra recorded cooling

from 300 K to 10 K. At low temperature, the emission maximum wavelength shifts to 480 nm due to the mitigation of self-absorption by the band narrowing (Supplementary Table 7). The inset shows the photoluminescence intensity increasing by +40% at below 100 K, which corresponds to an increment of the quantum yield up to ~0.60. This enhancement is larger than that expected considering the corresponding increment of the emission lifetime (Fig. 3b, inset). These findings suggest that additional temperature-dependent ultrafast quenching pathways of diffusing charges or molecular excitons are involved in the partial emission quenching³⁶. The presence of traps is supported by the variable-temperature radioluminescence experiments. The radioluminescence spectrum changes in accordance with the photoluminescence (Fig. 3c and Supplementary Table 7). On the other hand, the radioluminescence intensity—corrected by the photoluminescence behaviour (inset of Fig. 3b) to point out the intrinsic luminescence dependence on the temperature—is progressively reduced by a factor two at 10 K. This is a fingerprint of the presence of trapping sites, which compete with the recombination of diffusing free charges on emissive ligands. Thermal energy can free the trapped charges to be recovered for light generation reaching a thermal equilibrium (Supplementary Fig. 33)^{37,38}, but at low temperatures they are lost with a reduction of the emission intensity. The trap role in scintillation is investigated by wavelength-resolved thermally stimulated luminescence (TSL) measurements (Methods)^{39–41}. The smooth TSL glow curve—obtained by integrating the wavelength-resolved TSL spectra in the whole emission region—demonstrates the existence of a broad distribution of trap sites with different energy depths (Fig. 3d), which do not seriously affect the scintillation yield of the MOFs (Supplementary Fig. 34).

Radioactive gas detection with MOF powders

The capability of porous Hf-DPA to adsorb argon, krypton, xenon and radon at room temperature and concentrate their radioactive isotopes for detection was demonstrated by combined experimental and simulated approaches. Figure 4a shows the adsorption isotherms calculated by Grand Canonical Monte Carlo (GCMC) simulations (Methods and Supplementary Section 6). They successfully reproduce the experimental isotherms for argon and krypton, demonstrating the validity of the developed modelling as a predictive tool (Supplementary Figs. 35 and 36). The simulated adsorption at a given pressure shows a correlation between the amount of gas adsorbed and the atomic mass, with a preference for the heavier radon. The smaller gases such as krypton are more homogeneously distributed in all of the available space (Fig. 4b, left), whereas the larger radon atom is preferably hosted in the smaller tetrahedral cavities of the MOF (Fig. 4b, right), due to the more effective interactions between the gas molecules and the framework walls. The gas–matrix interaction energies (Supplementary Figs. 37 and 38) give insight into the affinity and retention capability of the framework towards the exploring gases (Fig. 4c), and have relevance for selectivity and detection applications in air. The gas diffusion modelled in the presence of air at room temperature indicates that krypton atoms pervade the entire MOF crystals within tens of microseconds, demonstrating that noble gas radionuclides could be rapidly adsorbed into the pores in standard working conditions (Supplementary Figs. 39 and 40).

The Hf-DPA has been tested using a radioactive krypton isotope (⁸⁵Kr) in a custom-made prototype device (Supplementary Fig. 41). The β -decay of ⁸⁵Kr produces electrons with a maximum emission energy of 687.1 keV and an average energy of 251.4 keV (ref. 42). The radionuclide can be mixed in air at different concentrations to tune the activity of the sample. The scintillation is detected by employing a time coincidence measurement technique based on the simultaneous use of two photomultiplier tubes (PMTs) (Fig. 1b, see Methods, Supplementary Section 11 and Supplementary Fig. 41)¹⁸. The technique can be applied using different coincidence windows to maximize the device's sensitivity^{43–45}. Here we tested a coincidence window of 40 ns (as used with liquid scintillators) and 400 ns. Figure 4d

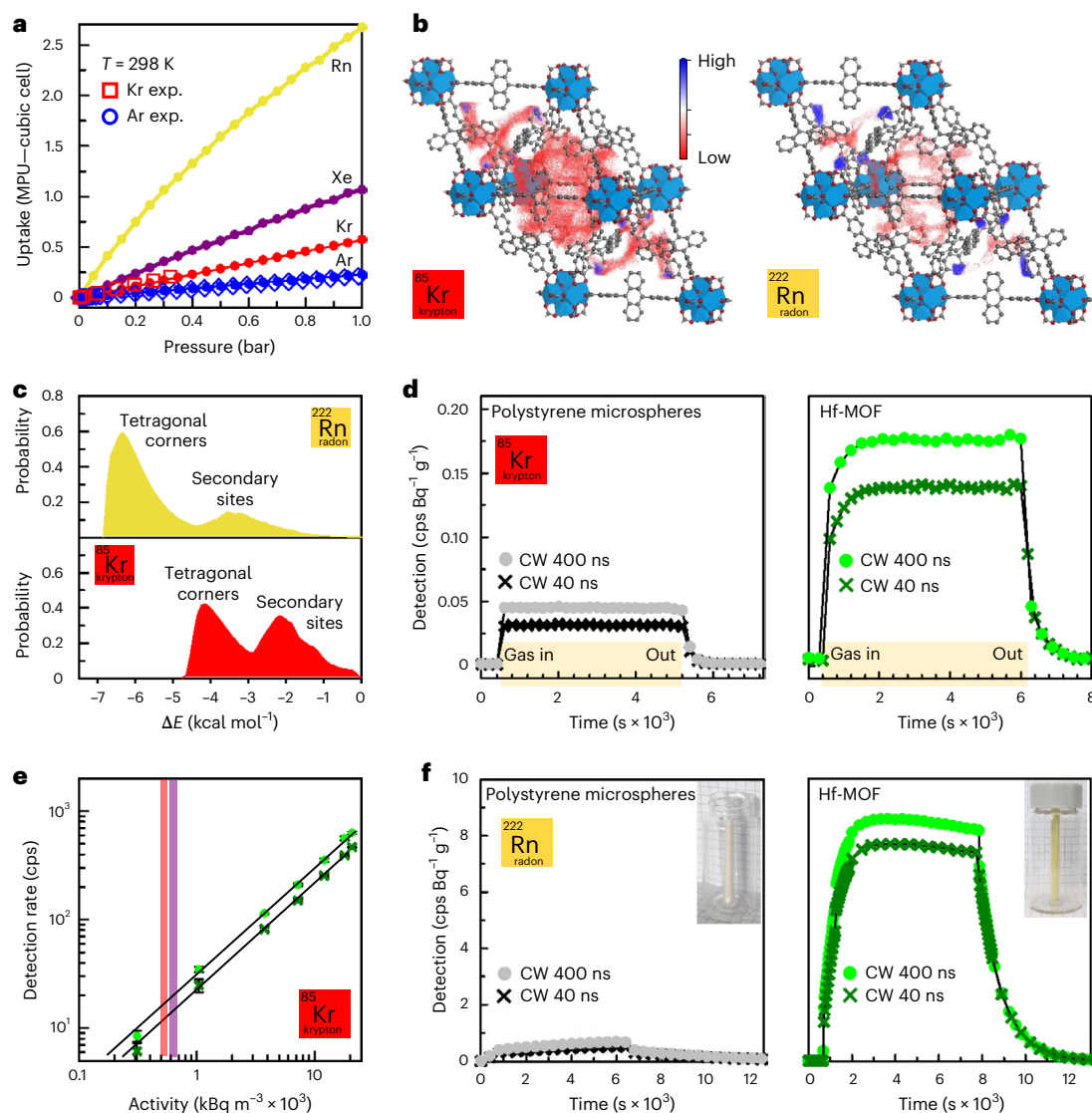


Fig. 4 | Radioactive gas adsorption and detection by porous scintillating Hf-DPA crystalline powder. **a**, Experimental argon and krypton isotherms and GCMC simulated adsorption isotherms of argon, krypton, xenon and radon for a cubic unit-cell of Hf-DPA ($32.79 \times 32.79 \times 32.79 \text{ \AA}^3$) at 298 K. The uptake is expressed in molecules per unit-cell (MPU). **b**, Gas density distributions calculated at room temperature at constant pressure of 50 mbar by GCMC adsorption simulations for krypton and radon. Blue and red colors indicate the highest and lowest gas density in the pores, respectively. **c**, Gas–matrix interaction energy distribution probability calculated at a constant pressure of 50 mbar and room temperature for krypton, xenon and radon. **d**, Double coincidence detection of ^{85}Kr by polystyrene microspheres powder and Hf-DPA

powder using two different coincidence windows (CWs) for detection (40 ns and 400 ns). The labels on the x-axis indicate when the radioactive gas has been injected into the detection device (gas in) and then washed out by a flux of clean air (gas out). cps, counts per second. **e**, Double coincidence detection rate of ^{85}Kr by the Hf-DPA powder as a function of the sample activity using different coincidence windows. The vertical lines mark the detection limit of a commercial device employed for detecting noble gas radionuclides (refs. 46,47, red and violet line, respectively). The solid lines are the fit of data with linear functions. Error bars depict the residual values of the fit. **f**, Double coincidence detection of ^{222}Rn by polystyrene microsphere powder and Hf-DPA powder using different coincidence windows.

shows the results obtained for detecting ^{85}Kr using a standard scintillating powder—that is, dye-doped polystyrene microspheres with diameters of $175 \pm 75 \text{ \mu m}$ (ref. 46)—and Hf-DPA. The data highlights an improved behaviour for porous crystals. First, Hf-DPA generates a scintillation intensity 4.6- and 3.9-times higher than microspheres for 40 ns and 400 ns coincidence windows, respectively. This demonstrates the efficiency of Hf-DPA as a scintillator despite its intrinsic lower density ($\sim 0.65 \text{ g cm}^{-3}$) compared with polystyrene (1.02 g cm^{-3}). Notably, gas detection can be performed with extremely high reproducibility ($\pm 1.3\%$ for 40 ns and $\pm 2.5\%$ for 400 ns coincidence windows, respectively). Moreover, the polystyrene emission peaked at 420 nm (Supplementary Fig. 31), wherein the PMTs detection efficiency (0.43)

is higher than for the 490 nm MOF emission (0.25)⁴⁷. A further improvement of the detection efficiency can therefore be envisaged by matching the scintillator and photodetector properties. Second, the expected increment using a longer coincidence window is less pronounced for Hf-DPA (around +25%) than for the polystyrene (around +50%). This indicates that MOFs work better as fast scintillators with a negligible slow emission contribution, giving a response closer to the ideal time-independent behaviour.

Third, the maximum scintillation signal is reached with slower kinetics for MOFs than polystyrene. The signal rise time—calculated as the time employed to reach 90% of the maximum plateau—is 600 s for Hf-DPA versus 100 s for microspheres. A similar effect is observed

when removing the radionuclides from the sample by purging with clean air. The scintillation switches off in 800 s for MOFs, whereas it takes half of the time for the polystyrene microspheres. These findings suggest that, in addition to the fast, automatic filling of interparticle space within packed microspheres, the radionuclides are adsorbed within the MOF pores, in agreement with the experimental and simulated adsorption tests, thus promoting the interaction of the β -radiation with the scintillators that results in a better performance.

The versatility of our approach was demonstrated by testing Hf-DPA crystals as detectors with other radionuclides of interest, namely ^{222}Rn (with its four decay daughters at the equilibrium, which are α - and high-energy β -emitters) and ^3H (Supplementary Figs. 41 and 42). Considering the larger capture of radon in the pores, the scintillation output should be improved with respect to krypton. Indeed, the detection efficiency is enhanced twentyfold with respect to polystyrene (Fig. 4f). Even for the elusive tritium, the MOF powder shows a better sensitivity in the detection counting rate—double that of polystyrene (Supplementary Fig. 43). This is a very important result as ^3H is one of the most difficult gas atoms to detect, given the relatively low energy of the β -radiation emitted with an average value of 5.7 keV (ref. 42). Regarding krypton, we further tested the device as a function of the activity of the sample, as a progressively greater number of sensitive detectors is required. As shown in Fig. 4e, we detected ^{85}Kr from an initial activity of 21 kBq m^{-3} , down to 0.3 kBq m^{-3} —two orders of magnitude lower. The instrumental response is linear with the sample activity, suggesting the possibility of setting highly accurate calibrations of devices to detect ultralow activity levels. Notably, we successfully detected an activity below the minimum value declared for commercial ^{85}Kr detectors (vertical lines in Fig. 4e), in a device much smaller in size, with less volume of monitored gas and using one-order-of-magnitude-shorter acquisition times (Methods and Supplementary Section 11), owing to the porous scintillator's ability to adsorb the gas^{48,49}. These remarkable results demonstrate that the prototype device presented here, although in its embryonal form, displays better sensitivity than state-of-the-art devices and highlights the technological advantage of potentially using compact, easy-to-handle and cheaper devices. Considering the good stability of Hf-DPA that does not imply any critical storage protocol (Supplementary Table 9 and Supplementary Fig. 45), this work strongly supports the development of radioactive gas detectors based on porous MOF crystals as scintillators that can overcome current technological limitations.

Discussion

In summary, we designed and fabricated specific scintillating porous MOF crystals to detect radioactive noble gases. Their good luminescence and scintillation properties—combined with their characteristic porosity—allowed us to realize a fully operative prototype detector. An intensive study on a broad range of critical β -emitting radioactive gases was performed, namely, the low-energy β -emitter ^3H , the high-energy β -emitter ^{85}Kr , and the β/α -emitter ^{222}Rn . The MOF crystals exhibited improved performance compared with commercial powder-like materials currently tested, and we found that ^{85}Kr can be detected with excellent sensitivity down to radioactivity values below the limit of commercial systems. The obtained results are therefore stimulating not only from the scientific point of view, as radionuclide detection using porous scintillators has been demonstrated here for the first time, but also from the technological perspective, hinting at a potential breakthrough by developing conceptually new optimized universal devices that allow detecting all the gas radionuclides species of interest. In this regard, it is worth pointing out that MOF powders cannot easily be used in the present form due to the practical problems of handling, especially from the perspective of industrial production. We are thus working on the realization of a hierarchical porous architecture in which porous MOFs are homogeneously distributed in a porous polymeric host endowed with

mesopores and macropores suitable for gas diffusion. In such a configuration, the MOFs will be employed to further concentrate and detect the radionuclides, thus realizing the first example of composite bulk porous scintillators for radioactive gas detection. Similarly, the instrumental design will be improved to get a more functional device. A possible evolution can be the use of a cylindrical shape container for the porous scintillator with aerosol filters as the entrance and exit face, in which the gas flow would circulate freely through the whole porous material, placed vertically between two photomultipliers. In such a configuration, the gas flow will be orthogonal to the detection line while diffusing through the whole scintillator, thus maximizing the radionuclide accumulation and the scintillation detection yield. The combination of easy-to-handle hierarchical porous scintillators and excellent detection properties of porous MOFs with an optimized instrumental design will provide a pivotal step forward in the fabrication of high-tech ultrasensitive and reusable detectors, especially for low-energetic radionuclides such as tritium produced in nuclear plants.

Online content

Any methods, additional references, Nature Portfolio reporting summaries, source data, extended data, supplementary information, acknowledgements, peer review information; details of author contributions and competing interests; and statements of data and code availability are available at <https://doi.org/10.1038/s41566-023-01211-2>.

References

1. Bollhöfer, A. et al. Half a century of Krypton-85 activity concentration measured in air over Central Europe: trends and relevance for dating young groundwater. *J. Environ. Radioact.* **205–206**, 7–16 (2019).
2. Zeng, J. et al. Development of a well-type phoswich detector for low concentration krypton-85 measurement. *Nucl. Instrum. Methods Phys. Res. A* **1013**, 165634 (2021).
3. Huang, Y.-J. et al. Automated separation and analysis of krypton-85 from low-volume gaseous effluent of nuclear power plant. *J. Radioanal. Nucl. Chem.* **323**, 213–222 (2020).
4. Aoyama, M. Long-term behavior of ^{137}Cs and ^3H activities from TEPCO Fukushima NPP1 accident in the coastal region off Fukushima, Japan. *J. Radioanal. Nucl. Chem.* **316**, 1243–1252 (2018).
5. Cao, Y. et al. Long-term investigation of environmental radioactivity levels and public health around the Qinshan Nuclear Power Plant, China. *Sci. Rep.* **12**, 4945 (2022).
6. Schoeppner, M. & Glaser, A. Present and future potential of krypton-85 for the detection of clandestine reprocessing plants for treaty verification. *J. Environ. Radioact.* **162–163**, 300–309 (2016).
7. *Comprehensive Nuclear-Test-Ban Treaty Organization* (CTBTO, 2022); <https://www.ctbto.org/>
8. Čujić, M. et al. Radon-222: environmental behavior and impact to (human and non-human) biota. *Int. J. Biometeorol.* **65**, 69–83 (2021).
9. Abd Elkader, M. M., Shinonaga, T. & Sherif, M. M. Radiological hazard assessments of radionuclides in building materials, soils and sands from the Gaza Strip and the north of Sinai Peninsula. *Sci. Rep.* **11**, 23251 (2021).
10. Rudin, C. M., Brambilla, E., Faivre-Finn, C. & Sage, J. Small-cell lung cancer. *Nat. Rev. Dis. Primers* **7**, 3 (2021).
11. Kissane, J., Neutze, J. A. & Singh, H. *Radiology Fundamentals: Introduction to Imaging and Technology* (Springer, 2020).
12. Camfferman, F. A. et al. Diagnostic and predictive value of Doppler ultrasound for evaluation of the brain circulation in preterm infants: a systematic review. *Pediatr. Res.* **87**, 50–58 (2020).

13. Nichols, A. L. Status of the decay data for medical radionuclides: existing and potential diagnostic γ emitters, diagnostic β^+ emitters and therapeutic radioisotopes. *Radiochim. Acta* **110**, 609–644 (2022).
14. European Union EURATOM Directive 59/2013 'Basic Safety Standards' (European Union, 2013); <https://eur-lex.europa.eu/eli/dir/2013/59/oj>
15. Legislative Decree of 31 July 2020, no. 101 of Implementation of the Directive 2013/59/EURATOM of the European Council (Ispettorato Nazionale per la Sicurezza Nucleare e la Radioprotezione, 2020); <https://www.isinucleare.it/en/radiation-protection-and-environmental-radioactivity>
16. Aprile, E., Bolotnikov, A. E., Bolozdynya, A. I. & Doke, T. *Noble Gas Detectors* (John Wiley and Sons, 2006).
17. Li, X. et al. Simultaneous determination of gross alpha/beta activities in water by liquid scintillation counting and its applications in the environmental monitoring. *Sci. Rep.* **12**, 8281 (2022).
18. Sabot, B., Dutsov, C., Cassette, P. & Mitev, K. Performance of portable TDCR systems developed at LNE-LNHB. *Nucl. Instrum. Methods Phys. Res. A* **1034**, 166721 (2022).
19. Eddaoudi, M., Li, H. & Yaghi, O. Highly porous and stable metal-organic frameworks: structure design and sorption properties. *J. Am. Chem. Soc.* **122**, 1391–1397 (2000).
20. Kitagawa, S., Kitaura, R. & Noro, S. I. Functional porous coordination polymers. *Angew. Chem. Int. Ed.* **43**, 2334–2375 (2004).
21. Férey, G. Hybrid porous solids: past, present, future. *Chem. Soc. Rev.* **37**, 191–214 (2008).
22. Mezenov, Y. A., Krasilin, A. A., Dzyuba, V. P., Nominé, A. & Milichko, V. A. Metal-organic frameworks in modern physics: highlights and perspectives. *Adv. Sci.* **6**, 1900506 (2019).
23. Elsaidi, S. K. et al. Radiation-resistant metal-organic framework enables efficient separation of krypton fission gas from spent nuclear fuel. *Nat. Commun.* **11**, 3103 (2020).
24. Jin, K., Lee, B. & Park, J. Metal-organic frameworks as a versatile platform for radionuclide management. *Coord. Chem. Rev.* **427**, 213473 (2021).
25. Lustig, W. P. et al. Metal-organic frameworks: functional luminescent and photonic materials for sensing applications. *Chem. Soc. Rev.* **46**, 3242–3285 (2017).
26. Doty, F., Bauer, C., Skulan, A., Grant, P. & Allendorf, M. Scintillating metal-organic frameworks: a new class of radiation detection materials. *Adv. Mater.* **21**, 95–101 (2009).
27. Perego, J. et al. Composite fast scintillators based on high-Z fluorescent metal-organic framework nanocrystals. *Nat. Photon.* **15**, 393–400 (2021).
28. Perego, J. et al. Highly luminescent scintillating hetero-ligand MOF nanocrystals with engineered Stokes shift for photonic applications. *Nat. Commun.* **13**, 3504 (2022).
29. Shi, W. et al. Advances of metal organic frameworks in analytical applications. *Mater. Today Adv.* **15**, 100273 (2022).
30. Yang, G. L., Jiang, X. L., Xu, H. & Zhao, B. Applications of MOFs as luminescent sensors for environmental pollutants. *Small* **17**, 2005327 (2021).
31. Sozzani, P. et al. Nanoporosity of an organo-clay shown by hyperpolarized xenon and 2D NMR spectroscopy. *Chem. Commun.* 1921–1923 (2006).
32. Comotti, A., Bracco, S., Valsesia, P., Ferretti, L. & Sozzani, P. 2D Multinuclear NMR, hyperpolarized xenon and gas storage in organosilica nanochannels with crystalline order in the walls. *J. Am. Chem. Soc.* **129**, 8566–8576 (2007).
33. Bassanetti, I. et al. Flexible porous molecular materials responsive to CO₂, CH₄ and Xe stimuli. *J. Mater. Chem. A* **6**, 14231–14239 (2018).
34. Comotti, A. et al. Fluorinated porous organic frameworks for improved CO₂ and CH₄ capture. *Chem. Commun.* **55**, 8999–9002 (2019).
35. Monguzzi, A. et al. Highly fluorescent metal-organic-framework nanocomposites for photonic applications. *Nano Lett.* **18**, 528–534 (2018).
36. Ding, T. X., Olshansky, J. H., Leone, S. R. & Alivisatos, A. P. Efficiency of hole transfer from photoexcited quantum dots to covalently linked molecular species. *J. Am. Chem. Soc.* **137**, 2021–2029 (2015).
37. Korzhik, M., Tamulaitis, G. & Vasil'ev, A. N. *Physics of Fast Processes in Scintillators*. Vol. 262 (Springer, 2020).
38. Guerassimova, N., Garnier, N., Dujardin, C., Petrosyan, A. & Pedrini, C. X-ray excited charge transfer luminescence of ytterbium-containing aluminium garnets. *Chem. Phys. Lett.* **339**, 197–202 (2001).
39. McKeever, S. W. S. *Thermoluminescence of Solids* (Cambridge Univ. Press, Cambridge 1985).
40. Vedda, A. et al. Trap-center recombination processes by rare earth activators in YAlO₃ single crystal host. *Phys. Rev. B* **80**, 045113 (2009).
41. Buryi, M. et al. Trapping and recombination centers in cesium hafnium chloride single crystals: EPR and TSL study. *J. Phys. Chem. C* **123**, 19402–19411 (2019).
42. Bé, M.-M. et al. *Table of Radionuclides (Vol. 3 – A = 3 to 244)* (International Bureau of Weights and Measures, 2006).
43. Dutsov, C., Cassette, P., Mitev, K. & Sabot, B. In quest of the optimal coincidence resolving time in TDCR LSC. *Nucl. Instrum. Methods Phys. Res. A* **987**, 164846 (2021).
44. Dutsov, C., Cassette, P., Sabot, B. & Mitev, K. Evaluation of the accidental coincidence counting rates in TDCR counting. *Nucl. Instrum. Methods Phys. Res. A* **977**, 164292 (2020).
45. Dutsov, C., Sabot, B., Cassette, P. & Mitev, K. Significance of the corrections for accidental coincidences in liquid scintillation counting measurements. *J. Radioanal. Nucl. Chem.* **331**, 3303–3311 (2022).
46. Santiago, L. M., Bagán, H., Tarancón, A. & Garcia, J. F. Synthesis of plastic scintillation microspheres: evaluation of scintillators. *Nucl. Instrum. Methods Phys. Res. A* **698**, 106–116 (2013).
47. *R7600U PMT* (Hamamtsu Photonics, 2022).
48. *FHT 59 E Noble Gas Monitor* (Thermo Scientific, 2022).
49. *XPR80* (Mirion Technologies, 2022).

Publisher's note Springer Nature remains neutral with regard to jurisdictional claims in published maps and institutional affiliations.

Open Access This article is licensed under a Creative Commons Attribution 4.0 International License, which permits use, sharing, adaptation, distribution and reproduction in any medium or format, as long as you give appropriate credit to the original author(s) and the source, provide a link to the Creative Commons license, and indicate if changes were made. The images or other third party material in this article are included in the article's Creative Commons license, unless indicated otherwise in a credit line to the material. If material is not included in the article's Creative Commons license and your intended use is not permitted by statutory regulation or exceeds the permitted use, you will need to obtain permission directly from the copyright holder. To view a copy of this license, visit <http://creativecommons.org/licenses/by/4.0/>.

© The Author(s) 2023

Methods

Synthesis of Hf-DPA crystals

Hf-DPA crystals were synthesized using modulated solvothermal condition. Briefly, 9,10-bis(4-carboxyphenyl) anthracene (209.0 mg; 0.5 mmol) and HfCl_4 (160.0 mg; 0.5 mmol) were added to a 100 ml pyrex bottle with cleavable teflon-lined cap. Dry DMF (50 ml) and 400 μl of formic acid were added and the bottle was closed and sonicated for 60 s to obtain a well-dispersed mixture. The mixture was heated at 120 °C for 22 h in a preheated oven. The glass bottle was then removed from the oven and cooled to room temperature. The yellowish solid was collected by filtration on a 0.2 μm PTFE membrane and washed with DMF (3×100 ml) and then CHCl_3 (3×100 ml). The powder was recovered and dried at 120 °C under high vacuum before further analysis. Yield: 178 mg (58%) (see the Supplementary Information for further details on ligand and MOF preparation).

Hf-DPA analysis and characterizations

Powder X-ray diffraction patterns were collected on a Rigaku Smartlab using Cu-K α radiation, whereas synchrotron radiation powder X-ray diffraction was performed at the ESRF ID22 beam line using a wavelength of 0.354 Å. The crystal structure was refined by the Rietveld method combined with molecular mechanics and plane-wave density functional theory calculations (Supplementary Section 5). The structure data are available at the Cambridge Crystallographic Data Centre repository, deposition no. 2218565. The composition of Hf-DPA was studied by means of NMR spectroscopy in solution, solid-state NMR spectroscopy, Fourier-transform infrared spectroscopy, thermogravimetric analysis, scanning electron microscopy and EDS analysis. The gas sorption properties were investigated collecting nitrogen, argon and krypton adsorption isotherms at 77 K up to saturation pressure and argon and krypton at 298 K; hyperpolarized ^{129}Xe NMR experiments were performed by a home-built apparatus with a continuous-flow delivery of hyperpolarized xenon gas with a Bruker Avance 300 spectrometer operating at a Larmor Frequency of 83.02 MHz for ^{129}Xe . The xenon and radon adsorption isotherms at 298 K were performed by GCMC.

Photoluminescence studies

Absorption spectra were recorded using a Cary Lambda 900 spectrophotometer at normal incidence with Suprasil quartz cuvettes with a 0.1 cm optical path length and an integrating sphere to eliminate scattering effects. Steady-state photoluminescence spectra were acquired using a Varian Eclipse fluorimeter (bandwidth 1 nm) using quartz cuvettes of 0.1 cm optical path length. Time-resolved photoluminescence spectra of the MOFs dispersions were recorded by monitoring the emission decay of the samples at 435 nm. The MOFs were excited with a pulsed light-emitting diode at 340 nm (3.65 eV, pulse width 80 ps; EP-LED 340, Edinburgh Instruments). The MOFs were excited with a pulsed laser at 405 nm (3.06 eV, pulse width 90 ps; EPL-405, Edinburgh Instruments) to avoid direct excitation of the host polymer matrix. photoluminescence decay times were measured at the maximum of the emission spectrum. Relative and absolute photoluminescence quantum yields were measured with different methods as described in the Supplementary Section 7. For experiments at cryogenic temperatures, the samples were excited by a frequency tripled pulsed Nd:YAG laser source at 3.49 eV (355 nm) operated at 10 kHz; the emitted light was collected using a custom apparatus featuring a liquid nitrogen-cooled, back-illuminated, and ultraviolet-enhanced charge-coupled device detector (Jobin-Yvon Symphony II) coupled to a monochromator (Jobin-Yvon Triax 180) equipped with a 100 lines per millimetre grating.

Radioluminescence and scintillation studies

The samples were excited by unfiltered X-ray irradiation using a Philips PW2274 X-ray tube, with a tungsten target, equipped with a beryllium window and operated at 20 kV. At this operating voltage, X-rays are

produced by the *Bremsstrahlung* mechanism, superimposed to the L and M transition lines of tungsten due to the impact of electrons generated through a thermionic effect and accelerated onto the tungsten target. Cryogenic radioluminescence measurements are performed in the 10–370 K interval. Radioluminescence has been recorded on powder samples of 1 mm thickness in an aluminium sample holder. For comparison the radioluminescence spectra has been normalized by the mass of the investigated powder.

Scintillation has been recorded under pulsed X-rays with energies up to 25 keV generated with a repetition rate of 1 MHz by a picosecond diode laser at 405 nm (Delta diode from Horiba) focused on an X-ray tube (model N5084 from Hamamatsu). The resulting photons were collected by Kymera spectrograph (ANDOR) and detected by a hybrid PMT 140-C from Becker and Hickl GmbH. For decay-time measurements, the photons were histogrammed using a PicoHarp300 time-correlated single-photon counting (32 ps time per bin) and for the time resolved spectra a MCS6A multiple-channel time analyzer was used (800 ps time per bin). Subnanosecond scintillation emission kinetics of the samples were measured with a time-correlated single-photon counting set-up.

Thermally stimulated luminescence measurements

Wavelength-resolved TSL at cryogenic temperatures is performed by using the same detection system as for radioluminescence measurements. Cryogenic TSL measurements are performed in the 10–320 K interval, with a linear heating rate of 0.1 K s $^{-1}$, after X-ray irradiation up to around 10 Gy. The dose values for X-ray irradiations were calibrated with an ionization chamber in air.

Radioactive gas detection experiments

The experiments are performed using a unique gas bench developed at the CEA, Paris-Saclay, and by allowing the production of radioactive gas atmospheres using high activity standards⁵⁰. Different sampling and dilution steps allow for precise control of the injected activity, and precise knowledge of the volumetric activity of each gas: at best, the relative standard uncertainty on the activity concentration is 0.4%, 0.6% and 0.8% for ^{222}Rn , ^{85}Kr and ^3H , respectively (Supplementary Table 9). For each experiment, the same type of three step sequence is performed. First, the measurement of the blank, by circulating clean air without additional radioactivity. Second, the measurement of scintillation by circulating the radioactive gas sample into the vial (4 mm diameter and 50 mm height, 0.1086 g for Hf-DPA and 0.3640 for polystyrene microspheres, activity 10 kBq). Third, circulation of clean air into the device to remove the radioactive gas. The light photons produced by scintillation are measured using a metrological device developed to exploit the triple-to-double coincidence ratio (Supplementary Fig. 41)¹⁸, with a specific connection cap adapted to the radioactive gas flow in the scintillator.

Data availability

The data that support the plots within this paper and other findings of this study are available from the corresponding author upon reasonable request, at the public repository of the project SPARTE FET Open Project (<https://www.sparte-project.eu/>). The Hf-DPA structure's Cambridge Crystallographic Data Centre deposition no. is 2218565. No custom code has been developed for computational modeling and simulations.

References

50. Sabot, B., Rodrigues, M. & Pierre, S. Experimental facility for the production of reference atmosphere of radioactive gases (Rn, Xe, Kr, and H isotopes). *Appl. Radiat. Isot.* **155**, 108934 (2020).

Acknowledgements

We acknowledge support from the European Community through the grant no. 899293, HORIZON 2020—SPARTE FET OPEN. Financial

support from the Italian Ministry of University (MUR) through grant no. PRIN 2020—SHERPA no. H45F2100343000, and from Lombardy Region through the ‘Enhancing photosynthesis’ award, no. H45F21002830007. We thank the ESRF synchrotron facility in Grenoble (France) for access to the ID22 beamline (project no. HC-4781).

Author contributions

M.O., F.C., A.V. and A.M. conceived and performed the photoluminescence, radioluminescence experiments. J.P., C.X.B., S.P., C.Da. and S.B. A.C. designed, synthesized and characterized the MOFs. C.Du. managed the scintillation experiments. B.S., S. P. and P.M. designed, performed and analyzed the gas detection experiments. C.Du., B.S., A.C. and AM. conceived the project and wrote the paper. A.C. and AM. wrote the paper. All of the authors agreed to all of the content of the manuscript, the author list and its order, and the author contribution statements. Any changes to the author list after submission will be subject to approval by all authors.

Competing interests

The authors declare no competing interests.

Additional information

Supplementary information The online version contains supplementary material available at <https://doi.org/10.1038/s41566-023-01211-2>.

Correspondence and requests for materials should be addressed to Anna Vedda, Angiolina Comotti or Angelo Monguzzi.

Peer review information *Nature Photonics* thanks Wei Chen, Wolfgang Heiss and the other, anonymous, reviewer(s) for their contribution to the peer review of this work.

Reprints and permissions information is available at www.nature.com/reprints.